Chromium Poisoning Mitigation Strategy in Strontium-Doped Lanthanum Manganite-Based Air Electrodes in Solid Oxide Fuel Cells

Michelle Sugimoto
Division of Materials Science and Engineering,
Boston University,
Boston, MA 02215
e-mail: msugi@bu.edu

Zhikuan Zhu
Department of Mechanical Engineering,
Boston University,
Boston, MA 02215
e-mail: zkzhu@bu.edu

Srikanth Gopalan
Division of Materials Science and Engineering;
Department of Mechanical Engineering,
Boston University,
Boston, MA 02215
e-mail: sgopalan@bu.edu

Soumendra Basu
Division of Materials Science and Engineering;
Department of Mechanical Engineering,
Boston University,
Boston, MA 02215
e-mail: basu@bu.edu

Uday B. Pal[1]
Division of Materials Science and Engineering;
Department of Mechanical Engineering,
Boston University,
Boston, MA 02215
e-mail: upal@bu.edu

Chromium poisoning of the air electrode remains an obstacle to the long-term performance of solid oxide fuel cells (SOFCs). In Sr-doped $LaMnO_3$ (LSM) air electrodes, the poisoning process results in two types of deposits, chromium oxide (Cr_2O_3), and Mn, Cr spinel ($MnCr_2O_4$). The former forms electrochemically and the latter forms via a chemical reaction. By applying a small anodic reverse bias, Cr_2O_3 deposits can be removed because their formation is electrochemical in nature. However, $MnCr_2O_4$ deposits remain because their formation is chemical, rather than electrochemical, in nature. In situ chemical decomposition of the Mn, Cr spinel was investigated as an alternate removal method as thermodynamics supports its decomposition into constituent oxides below ~540 °C in pure oxygen. The spinel decomposition process was characterized using thermogravimetric and X-ray diffraction analyses. The experimentally determined rate of spinel decomposition was undetectable (very slow) with isolated $MnCr_2O_4$ powders. The addition of 10 mol% gadolinia doped ceria (GDC) and silver powders significantly increased the rate of decomposition. However, the rate is limited by the diffusion of oxygen through the decomposed oxide layer. Although one strategy may be the addition of GDC and silver to the LSM air electrode to enhance spinel decomposition, the more effective mitigation strategy would be to prevent the formation of $MnCr_2O_4$ spinel in the first place through the removal of the reactants: Cr_2O_3 via electrochemical cleaning and mobile Mn ions in the zirconia electrolyte by incorporating a diffusion barrier layer such as GDC between the air electrode and electrolyte.
[DOI: 10.1115/1.4062192]

Keywords: chromium poisoning, Mn, Cr spinel, thermal gravimetric analysis, phase decomposition, analysis and design of components, devices, and systems, fuel cells, reliability, durability, and damage tolerance

Introduction

The long-term performance of solid oxide fuel cells (SOFC) remains afflicted by chromium poisoning, in which electrochemically active sites are blocked by Cr-rich species originating from chromium-containing interconnect and balance-of-plant components [1,2]. Various mitigation strategies have been explored including the use of Cr getters [3,4], Cr-tolerant electrode materials [5,6], and Cr-diffusion resistant interconnect coatings [7–9]. However, one strategy that has not been well explored is the recovery of cell performance post-degradation via removal of Cr-rich species. One such method that was recently validated for Sr-doped lanthanum manganate (LSM)—yttria-stabilized zirconia (YSZ) composite cells is electrochemical cleaning [10,11]. The application of a mild electrolytic bias oxidized Cr-rich deposits to form hexavalent Cr-containing vapor species (e.g., CrO_3). The freeing of electrochemically active sites yielded significant cell performance recovery. Cr_2O_3 deposits are removed during electrochemical cleaning because its formation is electrochemical in nature involving the reduction of CrO_3 (the most prevalent Cr-containing vapor species in dry air over the Cr-containing interconnects). The electrochemical deposition and removal of Cr_2O_3 occur according to the following half-cell reaction:

$$(\text{Removal})2CrO_3(g) + 6e^- \Leftrightarrow Cr_2O_3(s) + 3O^{2-}(\text{Deposition}) \quad (1)$$

This is depicted schematically in Fig. 1(*a*). Reduction of Cr-containing vapor species occurs at the electrochemically active sites, which in LSM-based cells is the YSZ/LSM/gas interface, or triple phase boundary (TPB). Deposition of Cr_2O_3 creates a new, less active TPB (YSZ/Cr_2O_3/gas) causing the propagation of the Cr_2O_3 layer along the YSZ surface [12].

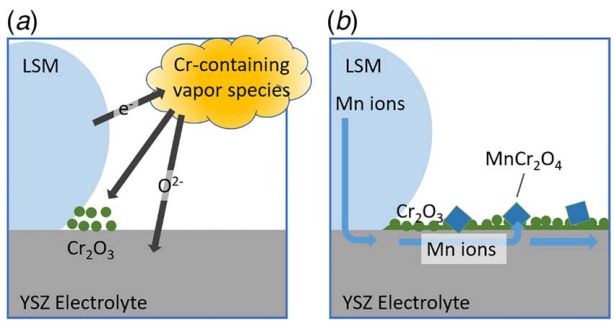

Fig. 1 (*a*) Electrochemical deposition of Cr_2O_3 and (*b*) chemical formation $MnCr_2O_4$ at the LSM/YSZ/gas interface under cathodic polarization

[1]Corresponding author.
Manuscript received December 14, 2022; final manuscript received March 21, 2023; published online April 17, 2023. Assoc. Editor: Naoki Shikazono.

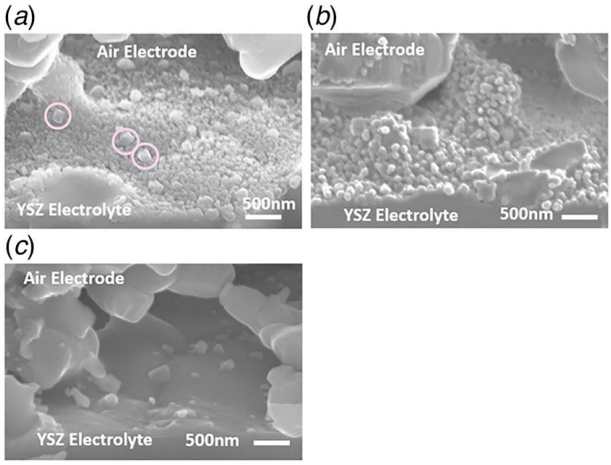

Fig. 2 SEM Micrographs of tested and fractured LSM/YSZ composite-based cells at the air electrode/electrolyte interface. All samples are tilted 30 deg to look down on the electrolyte surface. (*a*) Cell exposed to Cr-rich air flow for 120 h under 5% humidified air, 0.5 A/cm^2 at 800 °C. A few Mn, Cr spinel-type deposits are circled for reference. (*b*) Cell exposed to Cr-rich air flow for 50 h under 5% humidified air, 0.5 A/cm^2 at 800 °C. No Mn, Cr spinel-type deposits were identified. (*c*) Cell exposed to the same conditions as (*a*) followed by electrochemical cleaning for 2 h under 10% humidified air, 10% humidified fuel, −0.1 A/cm^2. Cr oxide-type deposits are removed, while Mn, Cr spinel deposits remain.

The second type of Cr-rich deposit that forms in LSM-based cells is $MnCr_2O_4$ (or Mn, Cr spinel). Unlike Cr_2O_3, $MnCr_2O_4$ forms via a chemical reaction and is thus not removed during electrochemical cleaning [10,11,13,14]. Cathodic polarization causes the migration of Mn ions from the LSM to the YSZ phase [10–12]. Mn ions then come into contact with electrochemically formed Cr_2O_3 and react to form $MnCr_2O_4$. Thus, both reactants, Cr_2O_3 and Mn, are supplied via cathodic polarization, and over time chemically react to form $MnCr_2O_4$ [15–17]. This is shown schematically in Fig. 1(*b*).

Support for these reaction mechanisms is found using scanning electron microscopy (SEM) images of fractured cell cross sections. Both deposit types are easily identified by their morphology (Fig. 2(*a*)). Mn, Cr spinel forms as larger, faceted deposits (circled in Fig. 2(*a*)). Cr oxide covers the remainder of the YSZ electrolyte surface as smaller, rounded deposits. Comparison between two cells subjected to identical Cr poisoning conditions (800 °C under 5% humidified air and 0.5 A/cm^2), but for different durations shows that the Mn, Cr spinel deposits are not observable via SEM imaging until sometime between 50 and 120 h (Figs. 2(*a*) and 2(*b*)). However, Cr_2O_3 deposits form with the onset of current flow.

Since the formation of Mn, Cr spinel is chemical as opposed to electrochemical in nature, electrochemical cleaning does not have the same effect as compared to Cr_2O_3. This is demonstrated using post-test SEM imaging comparing two cells Cr-poisoned under the same conditions: 120 h under Cr-rich, 5% humidified air, and 0.5 A/cm^2 at 800 °C (Figs. 2(*a*) and 2(*c*)) [10]. The second cell (Fig. 2(*c*)) was additionally subjected to electrochemical cleaning (2 h under 10% humidified air, 10% humidified fuel, and −0.1 A/cm^2), which clearly removed the Cr_2O_3 deposits from the electrolyte/air electrode interface, while the $MnCr_2O_4$ deposits were unaffected. This formation mechanism explains both why $MnCr_2O_4$ formation requires cathodic current and why electrochemical cleaning does not affect the Mn, Cr spinel deposits.

The formation of Mn, Cr spinel is detrimental to cell lifetime for two reasons. Of course, the formation of resistive spinel phases at the electrochemical reaction sites lowers cell performance. Second, the formation of Mn, Cr spinel depletes the LSM phase of manganese at the interface with YSZ. After a long-term operation, this can lead to loss of contact between LSM/YSZ particles [18]. Additionally, a higher La/Mn ratio in LSM leads to the formation of other unwanted resistive phases, namely $La_2Zr_2O_7$ [19], and makes the air electrode more susceptible to moisture.

As the Mn, Cr spinel is not affected by electrochemical cleaning, an alternate removal technique was investigated in the present work. In air, $MnCr_2O_4$ decomposes into its constituent oxides below ~480 °C (Fig. 3(*a*)). Cells with Cr deposition can be cooled below this temperature, allowing the $MnCr_2O_4$ to decompose. Then, the cells can be electrochemically cleaned at temperature to remove both the deposited and decomposed Cr oxide. Additionally, the decomposed Mn oxide may be reincorporated back into the YSZ lattice preventing any further loss of Mn from the LSM phase. Decomposition of the spinel can be facilitated by increasing the partial pressure of oxygen as this increases the decomposition temperature. Under pure oxygen, this is ~540 °C (Fig. 3(*b*)). Increasing this temperature is valuable when considering the thermal cycling and capacity factor of the system.

The phase diagrams in Figs. 3(*a*) and 3(*b*) indicate that the spinel ($2MnCr_2O_4(s)$) is not stable below 480 °C (in air) and 540 °C (in pure oxygen), respectively, and it dissociates into the constituent oxides, $Cr_2O_3(s)$ and $Mn_2O_3(s)$. The spinel reacts with oxygen and results in the formation of the constituent oxides according to the following decomposition reaction:

$$2MnCr_2O_4(s) + \frac{1}{2}O_2(g) \Leftrightarrow 2Cr_2O_3(s) + Mn_2O_3(s) \qquad (2)$$

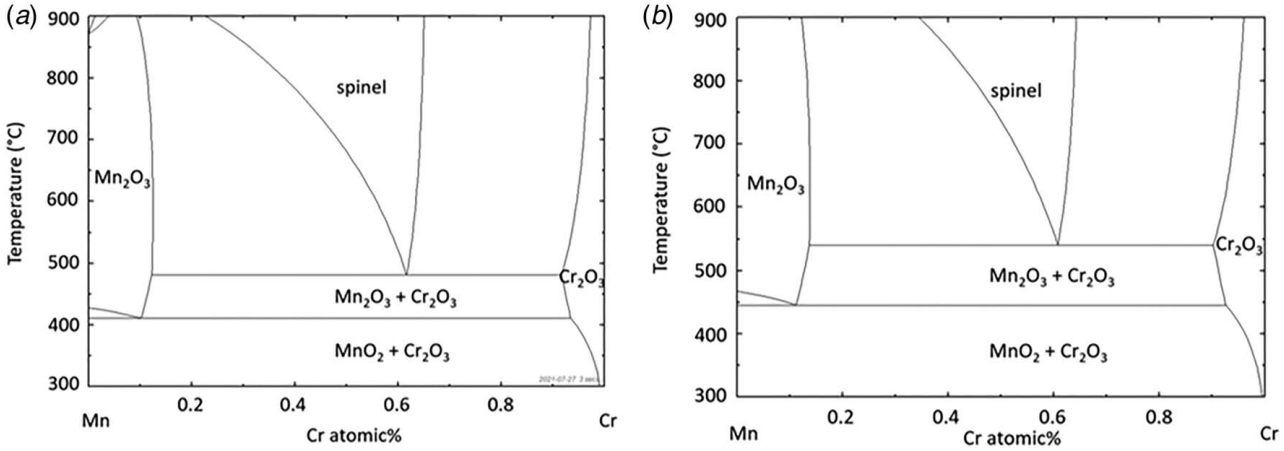

Fig. 3 Cr/Mn compositional phase diagram as a function of temperature under (*a*) air ($pO_2 = 0.21$) and (*b*) pure oxygen with a total pressure of 1 atm. Generated using FactSage.

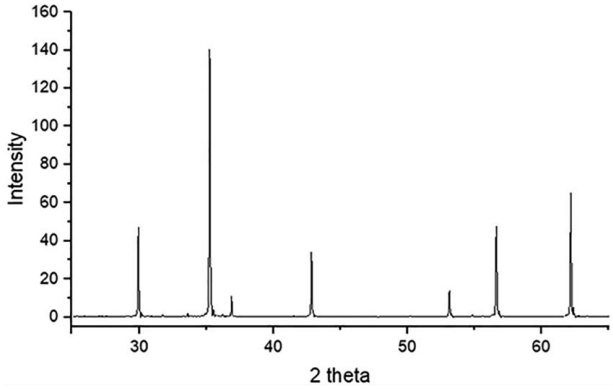

Fig. 4 XRD Spectra of synthesized $MnCr_2O_4$ spinel powders

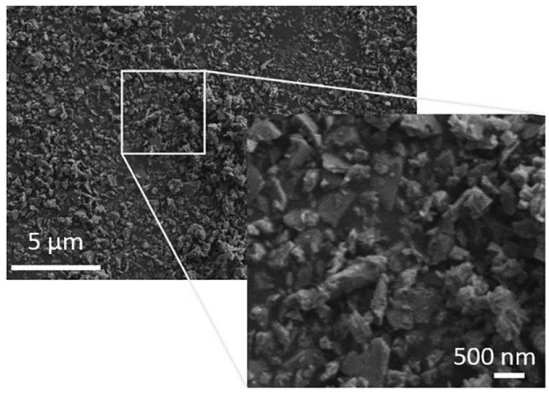

Fig. 5 SEM Micrograph of spex-milled $MnCr_2O_4$ spinel powders

Thus, thermogravimetric analysis (TGA) measuring the weight gain of prepared spinel powders in oxygen at 450 °C was used to estimate the rate of in situ spinel dissociation. In this study, TGA tests were designed to mimic conditions within the cell and to explore ways to accelerate the rate of spinel decomposition. This was accomplished by adjusting the particle size to match the spinel formed in the cell after 120 h of accelerated Cr poisoning (100–200 nm as seen in Figs. 2(*a*) and 2(*c*)). Additionally, the spinel powder was put into contact with materials having higher oxygen ion conductivity and electronic conductivity [20]. Here, $Gd_{0.1}Ce_{0.9}O_{1.95}$ (GDC10) and silver powders were used for higher ionic and electronic conductivities, respectively. In the cell system, the spinel phase is in contact with the YSZ electrolyte (high oxygen ion conductivity), and GDC10 which is a mixed ionic electronic oxide (MIEC) can be additionally added [21]. Additionally, silver is used in cell testing to lower contact resistance between leads and LSM electrodes. During cell testing, a very small fraction of the silver migrates to the LSM/YSZ interface [13,22]. Therefore, it was decided to add a small amount of silver to the spinel mix. Baseline tests with GDC10 and silver powders were also conducted to isolate the mass change due to spinel decomposition as well as to tease out contributions due to other material interactions.

Experimental Methods

$MnCr_2O_4$ spinel powders were synthesized via solid-state reaction. Stoichiometric ratios of the constituent oxides were ball-milled overnight in ethanol with 6.5 mm YSZ milling balls. The oxide powders were then dried and fired at 1200 °C for 5 h. Phase purity was verified using X-ray powder diffractometry (XRD), shown in Fig. 4 (Bruker D2). Spinel powders were spex-milled for 3 h using 0.3 mm YSZ milling media in ethanol to better match the size of spinel deposits formed in the cell after 120 h of accelerated Cr poisoning (Figs. 2(*a*) and 2(*c*)). The spex-milled particles were irregularly shaped, ranging in size from 100–600 nm (Fig. 5).

Three separate TGA runs were conducted, as well as four baseline runs, which are depicted in Fig. 6. B1 (Baseline 1) consisted of isolated spinel powders. B2 and B3 consisted of only pure GDC10 (fuel cell materials) and silver powders (Fisher Scientific, Hampton, NH), respectively. B4 consisted of a mixture GDC10 and silver powders, using the same amounts as in B2 and B3.

Run 1 consisted of a 60:40 volume ratio mixture of spinel and GDC10 powders. This mixture used the same amounts of spinel and GDC10 used in B1 and B2, respectively. Run 2 had the same volumetric ratio of powders as Run 1 but half the total mass.

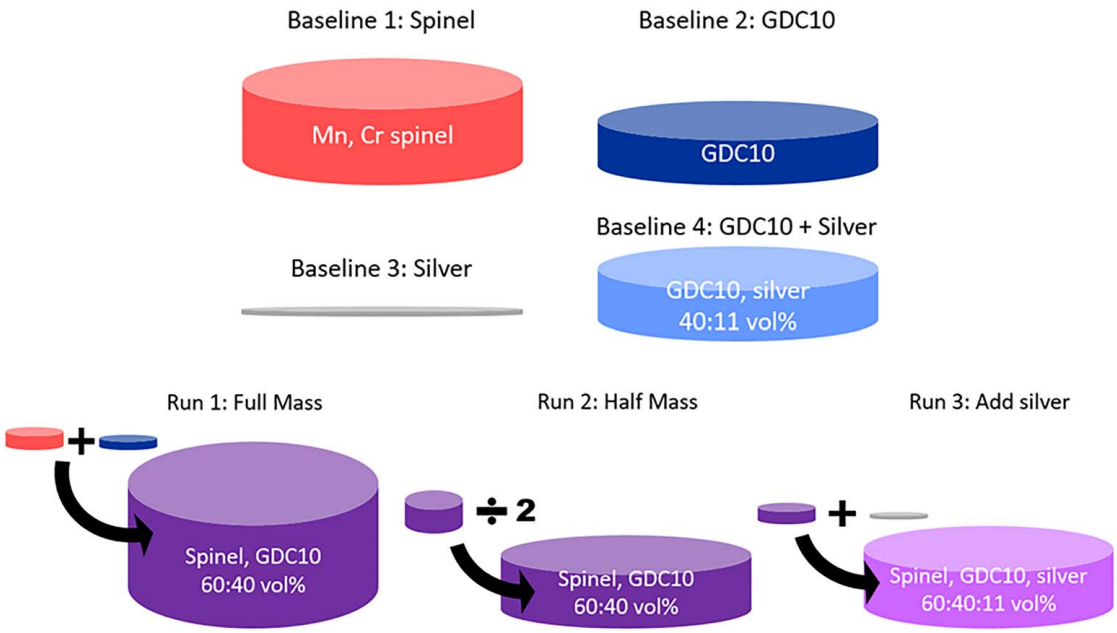

Fig. 6 TGA Ssample powder compositions. Tests conducted at 450 °C under 100 mL/min pure oxygen flow. Powder mixtures are depicted using color. Sizes depicted here are respective to volume.

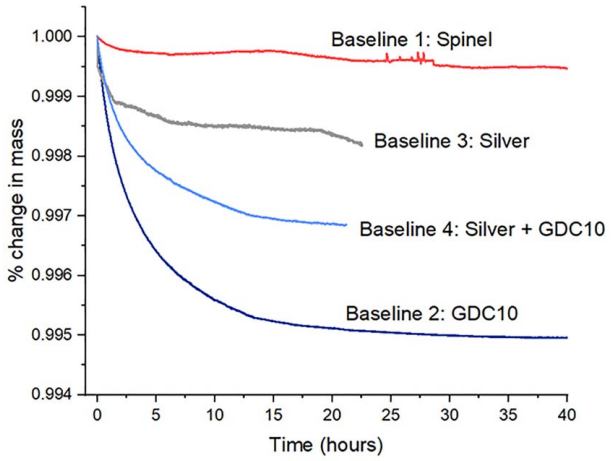

Fig. 7 Percent change in mass for baseline TGA runs operated at 450 °C under 100 mL/min pure oxygen flow

Comparison between Runs 1 and 2 indicates whether the reaction is occurring throughout the entire powder bed or is limited to the surface. Then, the rate measured here can be extrapolated to the significantly smaller amount of $MnCr_2O_4$ that forms in the cell ($\sim\mu$g) compared to the TGA samples ($\sim$mg). Run 3 compared to Run 2 tests the effect of silver addition. Both runs used the same amount of $MnCr_2O_4$ and GDC10 powders. The amount of silver added to Run 3 was the same as that used in B3 and B4.

Powders were loaded into alumina crucibles with a 5.67 mm inner diameter and height of 3.5 mm. Mass and temperature measurements were made using an SDT Q600 thermogravimetric analyzer (TA Instruments, New Castle, DE). Dried, pure oxygen has flowed over samples at a rate of 100 mL/min. Samples were heated to 450 °C using a ramp rate of 5 °C/min and left for $\sim$160 h.

Since the changes in mass were relatively small, slight changes in the ambient temperature ($\Delta T < 0.5$ °C) affected the mass reading. Thus, a run using a blank crucible was made to determine an appropriate coefficient to correct for the effects of temperature variation. This led to the following correction which was applied to all TGA runs:

$$m_{corrected} = m - (-0.1586 \cdot \Delta T) + offset \tag{3}$$

where T is the recorded temperature and m is the recorded mass measurement.

Results and Discussion

Baseline runs are normalized so that the changes in individual powder components are directly comparable (Fig. 7). No change was observed in B1 using isolated spinel powders. A significant decrease in GDC10 mass was observed in B2 as expected given the change in GDC10 oxygen non-stoichiometry as a function of temperature [23–25]. A slight mass loss was observed for silver in B3, which was attributed to the decomposition of a small amount of surface Ag_2O that had formed at room temperature. Interestingly, B4 (both silver and GDC10 powders) was not the sum change of the constituent components but rather fell between the two. There were in fact three equilibrium processes occurring in this sample: GDC10 oxygen non-stoichiometry, decomposition of Ag_2O to Ag, and dissolution of oxygen into silver [26–28]. The kinetics of oxygen dissolution into silver increased in B4 compared to B3 due to the catalytic effect coming from the high oxygen ion conductivity of GDC10 [20]. Overall, changes in mass due to spinel decomposition were isolated by subtracting out B2 from Runs 1 and 2 and B4 from Run 3. Baseline data were scaled to match the starting masses for the three runs.

Figure 8(*a*) shows the change in mass for Runs 1 and 2, along with B1 for comparison. The addition of GDC10 allowed for the detection of spinel decomposition, compared to isolated spinel powders in B1, which showed no change in mass. The addition of GDC10 may have increased the rate of spinel decomposition via two mechanisms. First, the high ionic conductivity of GDC10 aids in oxygen diffusion throughout the powder bed, increasing the total reaction area. Second, if the decomposition reaction involves an elementary charge transfer step, the GDC10 phase may aid as a catalyst (as suggested earlier for silver in B4). Again, the addition of GDC10 can mimic conditions within the

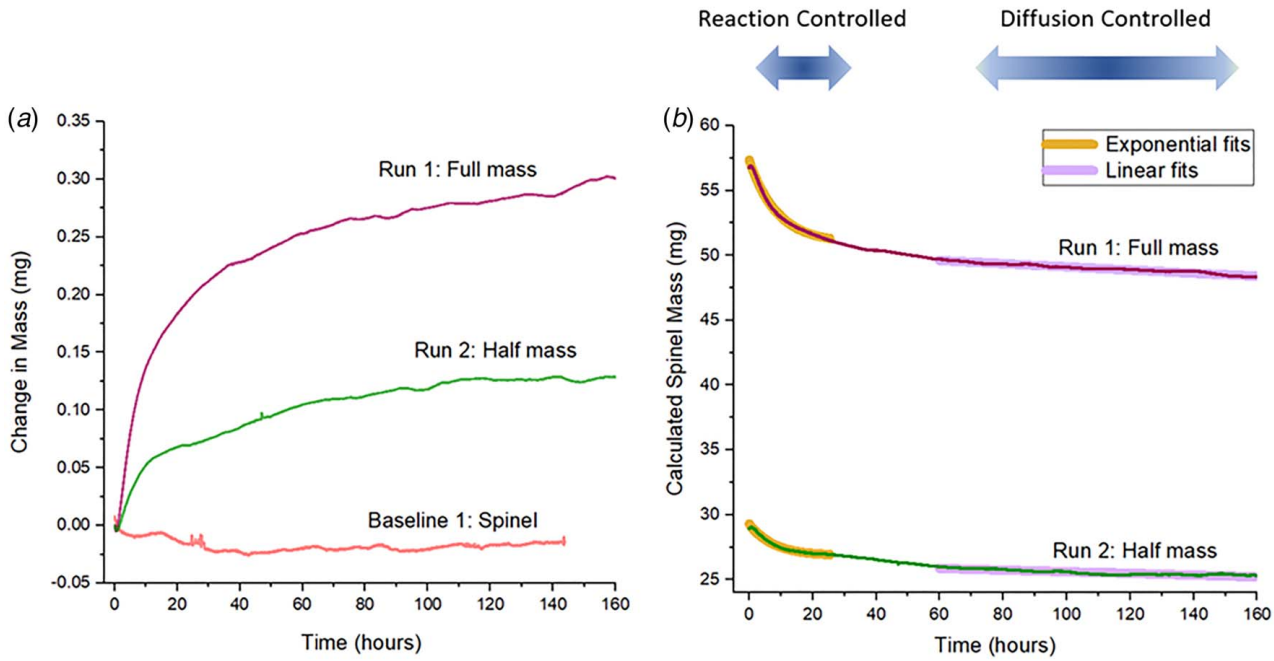

Fig. 8 (*a*) Change in mass (oxygen consumption) for Runs 1 and 2 and B1 (offset to zero). (*b*) Calculated change in spinel mass for Runs 1 and 2 with exponential fits 0–25 h and linear fits >60 h.

Table 1 Fit parameters for Runs 1 and 2

	Run 1: Full mass	Run 2: Half mass
0–25 h (reaction controlled)		
s (fit)	6.381	2.442
k (fit)	0.114	0.132
b (fit)	50.957	26.849
R-Square	0.9969	0.9948
s (calculated)	5.959	3.037
b (calculated)	50.796	25.887
>60 h (diffusion controlled)		
d (fit)	−0.0121	−0.0064
R-Square	0.9746	0.8344

cell where the formed $MnCr_2O_4$ deposits are in direct contact with the electrolyte, which is highly ionically conductive.

A comparison of Runs 1 (Full Mass) and 2 (Half Mass) shows that the change in mass was scaled by the total mass of the sample, indicating that the reaction occurred throughout the powder bed. The change in mass can be broadly divided into two regions. In the first ~25 h, the change in mass was well described by an exponential function suggesting a first-order reaction. After this, the change in mass tapered off until reaching a linear region at later times. To better understand the TGA results, the change in mass, i.e., oxygen incorporation, was related to the amount of $MnCr_2O_4$ in the sample using the starting masses and Eq. (2). The calculated spinel mass is plotted in Fig. 8(*b*). Now, the change in spinel mass during the first 25 h can be fit using a first-order reaction expression

$$m_{corrected} = s \cdot \exp(-kx) + b \tag{4}$$

where *s*, *k*, and *b* are parameters determined by the fit. These values are provided in Table 1. Both runs demonstrated a similar *k* value of ~0.12, which supports reaction-limited kinetics, where *k* is the reaction constant. The other two parameters, *s* and *b*, represent the "surface" and "bulk" areas of the particles, respectively. Thus, at short times, the rate is reaction-limited and the outer surface of the spinel particles decomposes unhindered. Once a layer of the Cr and Mn oxides forms at the particle surface, the rate of decomposition is limited by oxygen diffusion through this layer. The "surface" constituted roughly 10% of the total mass (dividing *s* by *b*). The thickness of the surface layer that best fits the output *s* and *b* values is 7 nm (assuming spherical spinel particles with a radius of 200 nm).

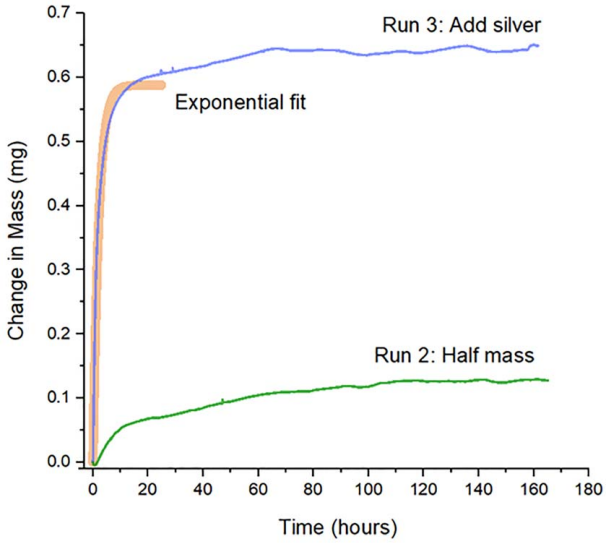

Fig. 10 Change in mass during Run 3. Fit using Eq. (4) from 0 to 25 h. Run 2 included for reference.

Meaning that the decomposition process was not inhibited by oxygen diffusion until the oxide layer reached ~7 nm in thickness, which is reasonable in comparison with other studies [29].

Directly after the reaction-limited region, there was a transition where both reaction and diffusion processes contributed to the rate of spinel decomposition. Diffusion through the oxide/spinel interface also likely played a role in this region [29]. At long times (>60 h), the data are well described by a line with a slope scaled by the starting $MnCr_2O_4$ mass, which aligns with a diffusion-limited process (Fig. 8(*b*)). The slope (*d*) and R-squared values for the linear fits are listed in Table 1.

To verify that spinel decomposition had occurred, forming Cr_2O_3 and Mn_2O_3, XRD measurements were acquired for the powder mixtures pre- and post-test. The XRD spectra for Runs 1 and 2 are shown in Fig. 9. Only peaks related to $MnCr_2O_4$ (blue circles) and GDC10 (green stars) were observed. No changes were observed before and after both TGA tests. Given the amount of Cr and Mn oxides that formed as evidenced by the change in mass, it is very likely that the crystalline domains of the oxide phases were too small to be detected by XRD.

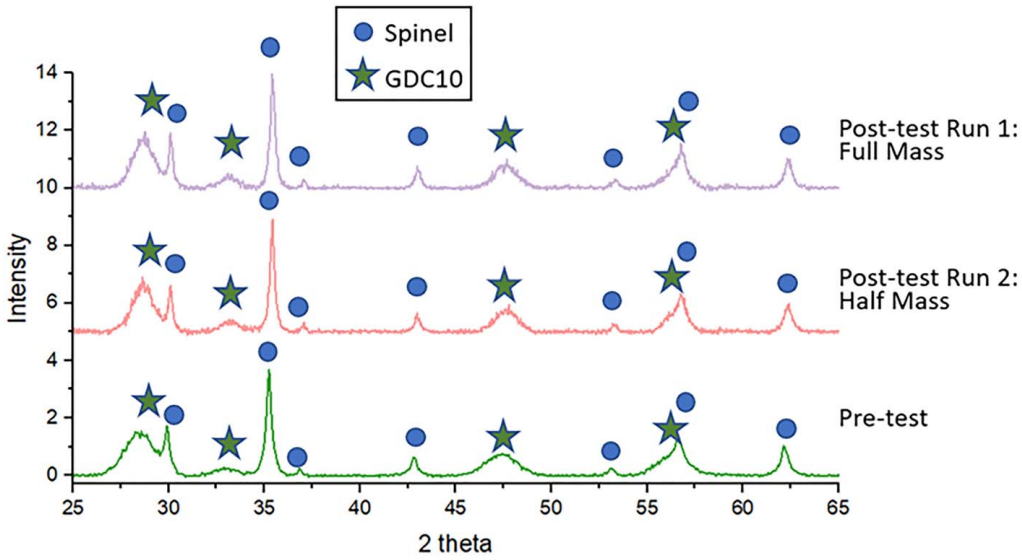

Fig. 9 XRD Spectra of mixed powders before and after Runs 1 and 2

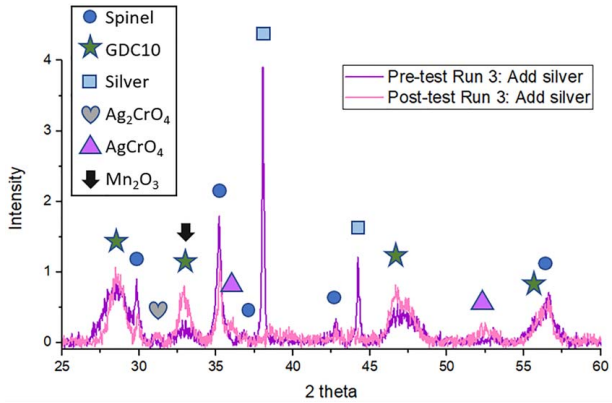

Fig. 11 XRD Measurements of mixed powders before and after Run 3. Pre-test shows strong silver peaks and post test shows silver chromate peaks and no pure silver peaks.

To increase the rate of spinel decomposition, the addition of a highly electronically conductive phase, silver, was investigated. The change in mass for Run 3 is shown in Fig. 10 along with Run 2 for comparison. The addition of silver resulted in a significant increase in mass. Further, the exponential fit at early times using Eq. (4) no longer described the data, suggesting that another process had occurred simultaneously. The XRD results (Fig. 11) revealed that Ag_2CrO_4 (gray hearts) and $AgCrO_4$ (purple triangles) were formed according to the following reactions:

$$Cr_2O_3(s) + 4Ag(s) + \frac{5}{2}O_2(g) \rightarrow 2Ag_2CrO_4(s) \quad (5)$$

$$Cr_2O_3(s) + 2Ag(s) + \frac{5}{2}O_2(g) \rightarrow 2AgCrO_4(s) \quad (6)$$

The formation of silver chromate species provided evidence that spinel decomposition occurred despite the absence of Cr_2O_3 peaks in the XRD spectra post-test. Further, it was clear that significantly more spinel decomposition had occurred in this run compared to Runs 1 and 2 from the decrease in spinel peak heights (blue circles) and the appearance of the major Mn_2O_3 peak (black arrow). The complete loss of Ag peaks was attributed to the formation of Ag chromates as well as a significant decrease in crystalline domain size which occurs at high oxygen partial pressure [26–28].

Additional TGA runs would be required to assign the mass gain in Run 3 to either spinel decomposition or the formation of silver chromates. However, it is clear that the addition of silver increased

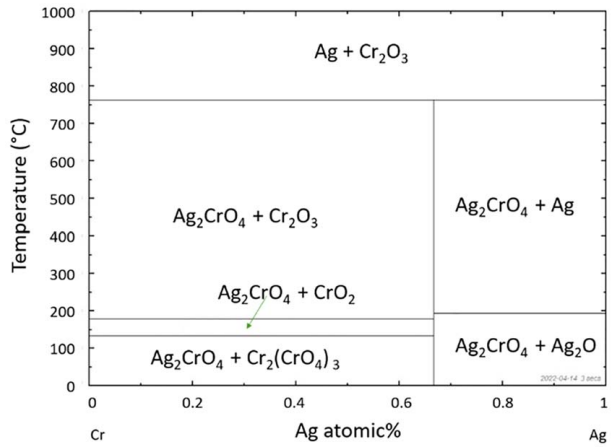

Fig. 12 Compositional phase diagram between Cr and Ag under 1 atm pure oxygen. Produced using FactSage.

the rate of spinel decomposition, as evidenced by the observable changes to the XRD spectrum. Further, the formation of Ag_2CrO_4 does not limit this method as it should decompose into Cr_2O_3 and Ag back at operating temperatures (Fig. 12). Thus, all decomposed Cr_2O_3 can then be removed via electrochemical cleaning.

The amount of spinel that forms in situ is significantly less than what was used for the TGA samples. However, since it was found that the rate of decomposition is independent of mass (comparing Runs 1 and 2), the in situ rate will be similar, which is to say quite slow. For optimized results, the size of the spinel deposits should be limited so that the "surface" (thickness ~ 7 nm) constitutes a significant portion of the total mass. Additionally, $MnCr_2O_4$ deposits should be left to decompose at 450 °C under pure oxygen for no longer than 25 h, since the rate after this point is considerably slower (diffusion limited). Given the rate of spinel decomposition and operational considerations, the best strategy is to prevent the formation of $MnCr_2O_4$ in the first place. One method to accomplish this is to remove Cr_2O_3 deposits via electrochemical cleaning before the significant formation of $MnCr_2O_4$. Another method that may be explored in future works is adding a barrier layer between the air electrode and electrolyte to prevent the formation of $MnCr_2O_4$. For example, doped ceria phases such as GDC demonstrate markedly lower Mn diffusivity compared to YSZ and are already commonly used in SOFC technologies [30].

Conclusions

Cr_2O_3-type deposits poison LSM-based air electrodes, but can be removed in situ via electrochemical cleaning. However, $MnCr_2O_4$ deposits remain because their formation is chemical, rather than electrochemical, in nature. Spinel decomposition, an alternate removal method, was demonstrated and characterized using TGA and XRD analyses. Mn, Cr spinel decomposes into its constitute oxides below ~540 °C in pure oxygen. The rate of spinel decomposition was undetectable with isolated spinel powders. The addition of GDC10 and silver powders significantly increased the rate of decomposition. However, the rate was still found to be too low to be practically feasible especially once it is limited by oxygen diffusion through the decomposed oxide layer. Thus, the more effective strategy is to prevent the formation of $MnCr_2O_4$ in the first place by removing reactants: Cr_2O_3, via electrochemical cleaning and Mn ions in YSZ by incorporating a diffusion barrier layer such as GDC between the air electrode and the zirconia electrolyte.

Acknowledgment

This work was supported, in part, by the U.S. Department of Energy, Office of Fossil Energy, under Award Number DE-FE0031206.

Conflict of Interest

There are no conflicts of interest.

Data Availability Statement

The data sets generated and supporting the findings of this article are obtainable from the corresponding author upon reasonable request.

References

[1] Horita, T., 2021, "Chromium Poisoning for Prolonged Lifetime of Electrodes in Solid Oxide Fuel Cells—Review," Ceram. Int., **47**(6), pp. 7293–7306.

[2] Zhou, L., Mason, J. H., Li, W., and Liu, X., 2020, "Comprehensive Review of Chromium Deposition and Poisoning of Solid Oxide Fuel Cells (SOFCs) Cathode Materials," Renewable Sustainable Energy Rev., **134**, p. 110320.

[3] Jiang, S. P., Zhang, S., and Zhen, Y. D., 2005, "Early Interaction Between Fe-Cr Alloy Metallic Interconnect and Sr-Doped $LaMnO_3$ Cathodes of Solid Oxide Fuel Cells," J. Mater. Res., **20**(3), pp. 747–758.
[4] Heo, S. J., Hong, J., Aphale, A., Hu, B., and Singh, P., 2019, "Chromium Poisoning of $La_{1-x}Sr_xMnO_{3\pm\delta}$ Cathodes and Electrochemical Validation of Chromium Getters in Intermediate Temperature-Solid Oxide Fuel Cells," J. Electrochem. Soc., **166**(13), pp. F990–F995.
[5] Harrison, C. M., Slater, P. R., and Steinberger-Wilckens, R., 2020, "A Review of Solid Oxide Fuel Cell Cathode Materials With Respect to Their Resistance to the Effects of Chromium Poisoning," Solid State Ionics, **354**, p. 115410.
[6] Sun, C., Hui, R., and Roller, J., 2010, "Cathode Materials for Solid Oxide Fuel Cells: A Review," J. Solid State Electrochem., **14**(7), pp. 1125–1144.
[7] Sun, Z., Gopalan, S., Pal, U. B., and Basu, S. N., 2017, "$Cu_{1.3}Mn_{1.7}O_4$ Spinel Coatings Deposited by Electrophoretic Deposition on Crofer 22 APU Substrates for Solid Oxide Fuel Cell Applications," Surf. Coat. Technol., **323**, pp. 49–57.
[8] Tan, K. H., Rahman, H. A., and Taib, H., 2019, "Coating Layer and Influence of Transition Metal for Ferritic Stainless Steel Interconnector Solid Oxide Fuel Cell: A Review," Int. J. Hydrogen Energy, **44**(58), pp. 30591–30605.
[9] Shaigan, N., Qu, W., Ivey, D. G., and Chen, W., "A Review of Recent Progress in Coatings, Surface Modifications and Alloy Developments for Solid Oxide Fuel Cell Ferritic Stainless Steel Interconnects," J. Power Sources, **195**(6), pp. 1529–1542.
[10] Zhu, Z., Sugimoto, M., Pal, U., Gopalan, S., and Basu, S., 2020, "Electrochemical Cleaning: An In-Situ Method to Reverse Chromium Poisoning in Solid Oxide Fuel Cell Cathodes," J. Power Sources, **471**, p. 228474.
[11] Zhu, Z., Sugimoto, M., Pal, U., Gopalan, S., and Basu, S., 2020, "Multiple Cycle Chromium Poisoning and In-Situ Electrochemical Cleaning of LSM-Based Solid Oxide Fuel Cell Cathodes," J. Power Sources Adv., **6**, p. 100037.
[12] Paulson, S. C., and Birss, V. I., 2004, "Chromium Poisoning of LSM-YSZ SOFC Cathodes," J. Electrochem. Soc., **151**(11), p. A1961.
[13] Sugimoto, M., 2022, "Chromium Poisoning Mitigation in Solid Oxide Fuel Cell Air Electrodes: Mechanisms for Cr Deposition and Removal," Dissertation, Boston University, Boston, MA.
[14] Zhu, Z., 2022, "Mitigation of Chromium Poisoning in Solid Oxide Fuel Cell Cathodes," Dissertation, Boston University, Boston, MA.
[15] Backhaus-Ricoult, M., Adib, K., St.Clair, T., Luerssen, B., Gregoratti, L., and Barinov, A., 2008, "In-Situ Study of Operating SOFC LSM/YSZ Cathodes Under Polarization by Photoelectron Microscopy," Solid State Ionics, **179**(21–26), pp. 891–895.
[16] Huber, A. K., Falk, M., Rohnke, M., Luerssen, B., Amati, M., Gregoratti, L., Hesse, D., and Janek, J., 2012, "In Situ Study of Activation and De-Activation of LSM Fuel Cell Cathodes—Electrochemistry and Surface Analysis of Thin-Film Electrodes," J. Catal., **294**, pp. 79–88.
[17] Norrman, K., Hansen, K. V., and Jacobsen, T., 2015, "Dynamic Behavior of Impurities and Native Components in Model LSM Microelectrodes on YSZ," RSC Adv., **5**(106), pp. 87679–87693.
[18] Nielsen, J., and Mogensen, M., 2011, "SOFC LSM:YSZ Cathode Degradation Induced by Moisture: An Impedance Spectroscopy Study," Solid State Ionics, **189**(1), pp. 74–81.
[19] Jiang, S. P., Love, J. G., Zhang, J. P., Hoang, M., Ramprakash, Y., Hughes, A. E., and Badwal, S. P. S., 1999, "Electrochemical Performance of LSM/Zirconia-Yttria Interface as a Function of A-Site Non-Stoichiometry and Cathodic Current Treatment," Solid State Ionics, **121**(1), pp. 1–10.
[20] Milshtein, J. D., Gergel, D. R., Basu, S. N., Pal, U. B., and Gopalan, S., 2015, "Mixed Ionic Electronic Conducting Powder Bed for Grid Level Energy Storage and Release: A Study of Tungsten Oxide Reduction Kinetics," Int. J. Hydrogen Energy, **40**(9), pp. 3624–3632.
[21] Shi, H., Su, C., Ran, R., Cao, J., and Shao, Z., 2020, "Electrolyte Materials for Intermediate-Temperature Solid Oxide Fuel Cells," Prog. Nat. Sci. Mater. Int., **30**(6), pp. 764–774.
[22] Jaiswal, A., and Wachsman, E. D., 2006, "Direct Current Bias Studies on $(Bi_2O_3)_{0.8}(Er_2O_3)_{0.2}$ Electrolyte and Ag-$(Bi_2O_3)_{0.8}(Er_2O_3)_{0.2}$ Cermet Electrode," Solid State Ionics, **177**(7–8), pp. 677–685.
[23] Bishop, S. R., Duncan, K. L., and Wachsman, E. D., 2009, "Defect Equilibria and Chemical Expansion in Non-Stoichiometric Undoped and Gadolinium-Doped Cerium Oxide," Electrochim. Acta, **54**(5), pp. 1436–1443.
[24] Mogensen, M., Sammes, N. M., and Tompsett, G. A., 2000, "Physical, Chemical and Electrochemical Properties of Pure and Doped Ceria," Solid State Ionics, **129**(1–4), pp. 63–94.
[25] Wang, S., Inaba, H., Tagawa, H., Dokiya, M., and Hashimoto, T., 1998, "Nonstoichiometry of $Ce_{0.9}Gd_{0.1}O_{1.95-x}$," Solid State Ionics, **107**(1–2), pp. 73–79.
[26] Al-Kuhaili, M. F., 2007, "Characterization of Thin Films Produced by the Thermal Evaporation of Silver Oxide," J. Phys. D: Appl. Phys., **40**(9), pp. 2847–2853.
[27] Djokić, S. S., Burrell, R. E., Le, N., and Field, D. J., 2001, "An Electrochemical Analysis of Thin Silver Films Produced by Reactive Sputtering," J. Electrochem. Soc., **148**(3), pp. C191–C196.
[28] Gao, X. Y., Wang, S. Y., Li, J., Zheng, Y. X., Zhang, R. J., Zhou, P., Yang, Y. M., and Chen, L. Y., 2004, "Study of Structure and Optical Properties of Silver Oxide Films by Ellipsometry, XRD and XPS Methods," Thin Solid Films, **455–456**, pp. 438–442.
[29] Finsterbusch, M., Lussier, A., Negusse, E., Zhu, Z., Smith, R. J., Schaefer, J. A., and Idzerda, Y. U., 2010, "Effect of Cr_2O_3 on the ^{18}O Tracer Incorporation in SOFC Materials," Solid State Ionics, **181**(13–14), pp. 640–645.
[30] He, S., Chen, K., Saunders, M., Li, J., Cui, C. Q., and Jiang, S. P., 2017, "A FIB-STEM Study of $La_{0.8}Sr_{0.2}MnO_3$ Cathode and Y_2O_3-ZrO_2/Gd_2O_3-CeO_2 Electrolyte Interfaces of Solid Oxide Fuel Cells," J. Electrochem. Soc., **164**(13), pp. F1437–F1447.